



The sensitivity of the atmospheric branch of the global water cycle to temperature fluctuations at synoptic to decadal time-scales in different satellite- and model-based products

Miguel Nogueira¹

Received: 4 October 2017 / Accepted: 22 February 2018 / Published online: 28 February 2018
© Springer-Verlag GmbH Germany, part of Springer Nature 2018

Abstract

Spectral analysis of global-mean precipitation, P , evaporation, E , precipitable water, W , and surface temperature, T_s , revealed significant variability from sub-daily to multi-decadal time-scales, superposed on high-amplitude diurnal and yearly peaks. Two distinct regimes emerged from a transition in the spectral exponents, β . The weather regime covering time-scales $< \sim 10$ days with $\beta \geq 1$; and the macroweather regime extending from a few months to a few decades with $0 < \beta < 1$. Additionally, the spectra showed a generally good statistical agreement amongst several different model- and satellite-based datasets. Detrended cross-correlation analysis (DCCA) revealed three important results which are robust across all datasets: (1) Clausius–Clapeyron (C–C) relationship is the dominant mechanism of W non-periodic variability at multi-year time-scales; (2) C–C is not the dominant control of W , P or E non-periodic variability at time-scales below about 6 months, where the weather regime is approached and other mechanisms become important; (3) C–C is not a dominant control for P or E over land throughout the entire time-scale range considered. Furthermore, it is suggested that the atmosphere and oceans start to act as a single coupled system at time-scales $> \sim 1$ – 2 years, while at time-scales $< \sim 6$ months they are not the dominant drivers of each other. For global-ocean and full-globe averages, ρ_{DCCA} showed large spread of the C–C importance for P and E variability amongst different datasets at multi-year time-scales, ranging from negligible (< 0.3) to high (~ 0.6 – 0.8) values. Hence, state-of-the-art climate datasets have significant uncertainties in the representation of macroweather precipitation and evaporation variability and its governing mechanisms.

Keywords Global water cycle · Clausius–Clapeyron · Multiscale analysis · Climate sensitivity · Detrended cross-correlation analysis · Climate variability

1 Introduction

The sensitivity of the global hydrological cycle to surface temperature variations is a critical question to understand and assess the impacts of climate change on water and energy balances. Despite some significant advances, the problem remains largely open reflecting the currently limited understanding of the relationships that exist among key components of the water cycle on various spatial and temporal scales.

An important mechanism for the global hydrological cycle variability is the Clausius–Clapeyron (C–C)

relationship, which establishes a direct link between atmospheric saturation vapor pressure, e_s , and temperature, T :

$$\frac{d \ln e_s}{dT} = \frac{L}{RT^2} \equiv \alpha(T), \quad (1)$$

where L is the latent heat of vaporization and R is the gas constant. At temperatures typical of the lower troposphere in the present climate, the saturation vapor pressure increases by about 7% for a 1 – K increase in temperature, i.e. $\alpha \approx 0.07 \text{ K}^{-1}$. Assuming constant relative humidity, the C–C relation further implies that the fractional change in global mean atmospheric precipitable water ($\delta W/W$) is proportional to temperature fluctuations, δT , with a scaling ratio of about $7\% \text{ K}^{-1}$ (see e.g. Held and Soden 2006):

$$\frac{\delta W}{W} \approx \alpha \delta T, \quad (2)$$

✉ Miguel Nogueira
mdnogueira@fc.ul.pt

¹ Instituto Dom Luiz, Faculdade de Ciências da Universidade de Lisboa, Campo Grande, 1749-016 Lisbon, Portugal

Numerous studies have provided a robust confirmation for the linear relationships between fluctuations of global-averaged W and T at multi-decadal to centennial time-scales, and have also reported a similar direct proportionality between changes in precipitation ($\delta P/P$) and δT (e.g. Boer 1993; Betts 1998; Trenberth 1998, 2011; Wentz and Schabel 2000; Allen and Ingram 2002; Trenberth et al. 2005; Held and Soden 2006; Gu et al. 2007; Wentz et al. 2007; Adler et al. 2008, 2017; Stephens and Ellis 2008; Allan et al. 2010; Schneider et al. 2010; O’Gorman and Muller 2010; Liu and Allan 2012; Singleton and Toumi 2013). However, while the C–C ($\sim 7\%/K$) scaling seems to apply to changes in global-mean atmospheric water vapor at very long time-scales, large spread has been reported for the global-mean precipitation sensitivity to temperature, typically estimated to be in the 1–3%/K. One admitted explanation for this discrepancy between W and P sensitivity to T is the radiative constraint imposed by outgoing long-wave radiation that must radiate back to space the latent heat associated with precipitation (Allen and Ingram 2002; Stephens and Ellis 2008). Similar arguments can be used for the sensitivity of global-mean evaporation to temperature, which should not differ vastly from 1 to 3%/K quoted above, as they are also strongly energetically constrained (see e.g. Schneider et al. 2010; Trenberth 2011).

If the C–C relationship was the dominant mechanism of global-mean W , P or E variation with temperature, then these time-series could be expected to display strong correlations to the global-mean surface temperature (T_s) time-series. Gu and Adler (2011, 2012) used satellite-based observations (complemented by a reanalysis product for W over land) and found very high correlations between the inter-annual variability of global-averaged W and T_s , in agreement with the C–C relationship. The high correlation values held when global-ocean or global-land averages were considered. Additionally, they reported much weaker (but significant) correlations between P and T_s at inter-annual time-scales over the full globe and global ocean, and non-significant correlation values (< 0.3) when global-land averaged time-series were considered. However, the information provided by correlations estimated at a single time-scale is insufficient, since it is a well-known fact that time-series of precipitation and other relevant atmospheric variables (including temperature, atmospheric moisture and wind) display a complex variability structure over a wide range of temporal scales (e.g. Pelletier 2002; Fraedrich and Blender 2003; Huybers and Curry 2006; Rybski et al. 2008; Vyushin and Kushner 2009; Vyushin et al. 2009; Lovejoy and Schertzer 2013; Lovejoy 2015; de Lima and Lovejoy 2015; Henriksson et al. 2015; Fredriksen and Rypdal 2016; Nogueira 2017a). Furthermore, this complex multiscale structure has been shown to play a role (at least) as important as the large amplitude periodic components (diurnal and seasonal) for many atmospheric variables (e.g., Lovejoy 2015;

Nogueira 2017a). However, a deep understanding of the underlying governing mechanisms at different time-scales remains largely elusive. In this sense, the statistical relationship between various atmospheric fields as a function of time-scale is an important but often neglected topic.

The detrended cross-correlation analysis (DCCA), first proposed by Podobnik and Stanley (2008), allows to accurately quantify power-law correlations between two different time-series over wide ranges of time-scales. Recently, Piao and Fu (2016) employed DCCA to daily near-surface temperature and relative humidity time-series obtained from four stations located in China. They found different signs of correlation between monthly and annual time-scales, which they associated to different governing processes. Subsequently, Nogueira (2017b) employed DCCA to satellite-based and reanalysis datasets and found that precipitation over the wettest regions on the planet (the Intertropical Convergence Zone and the Atlantic and Pacific storm-tracks) displays tight correlations with moisture divergence at monthly to decadal time-scales, but barely no correlation to local surface temperature, i.e. the regional precipitation over the wettest regions is governed by dynamics, not thermodynamics. Lovejoy et al. (2017) used a Haar fluctuations to show that the coupling of air temperature fluctuations over land and SST abruptly changes from very low to very high at time-scales larger than about 1–2 years. Building on these recent works, the present investigation uses DCCA to explore the statistical relations between the global water cycle (namely W , P and E time-series) and T_s over a wide range of time-scales (from a few days to about a decade), considering several state-of-the-art observational and model-based (including reanalysis) datasets. The goal is to provide further clues to the understanding of its complex multi-scale structure and the associated physical mechanisms, focusing particularly on the role of the C–C relationship. Simultaneously, a comparison of the global water cycle variability in the different climate datasets considered is presented under a multi-scale framework. The datasets and the multiscale analysis methodologies considered in the present manuscript are presented in Sect. 2. The results are presented in Sect. 3, including the multiscale spectral analysis of W , P , E and T_s variability over the full globe, global ocean and global land, and an application of DCCA to study sensitivity of global water cycle time-series to temperature fluctuations. Finally, the main results are summarized and discussed in Sect. 4.

2 Data and methodology

2.1 Datasets

In the present investigation, gridded datasets of monthly average surface temperatures were obtained from the Hadley Centre and the Climatic Research Unit (HadCRUT) version

4.5 (Morice et al. 2012) and from Goddard Institute for Space Studies (GISSTEMP) analysis (Hansen et al. 2010). The HadCRUT dataset covers the globe at 5° resolution, from 1850 to present, and the values are provided as anomalies relative to the 1961–1990 reference period. This dataset is a blend of the CRUTEM4 land surface air temperature dataset and the HadSST3 sea surface temperature (SST) dataset. The GISSTEMP covers the globe at 2° resolution, from 1880 to the present, and the values are provided as anomalies relative to the 1951–1980 reference period. The GISSTEMP analysis specifies the temperature anomaly at a given location as the weighted average of the anomalies for all stations located within 1200 km of that point, with the weight decreasing linearly from unity for a station located at that point to zero for stations located 1200 km or farther from the point in question (Hansen et al. 2010).

Precipitable water observations were obtained from Remote Sensing Systems (RSS) Special Sensor Microwave Imager (SSM/I) version-7, extending from 1988 to present (Wentz 1997; Wentz et al. 2007). This is a monthly dataset covering the ice-free ocean areas at 1° resolution, constructed by intercalibrating the measurements from several different satellites for each channel at the radiance level, and then using a common algorithm to retrieve the precipitable water.

Rainfall observations were obtained from the Global Precipitation Climatology Project (GPCP) version 2.3 monthly precipitation dataset (Adler et al. 2003), which covers the globe at 2.5° resolution from 1979 to the present. GPCP is produced by merging a variety of data sources, including passive microwave-based rainfall retrievals from the SSM/I and the special sensor microwave imager sounder (SSMIS), infrared (IR) rainfall estimates from geostationary and polar-orbiting satellites, and surface rain gauges.

Rainfall observations were also obtained from the Climate Prediction Center (CPC) Merged Analysis of Precipitation (CMAP) monthly precipitation dataset (Xie and Arkin 1997), which covers the globe at 2.5° resolution from 1979 to present. The values are obtained from rain gauge data combined with five kinds of satellite estimates—SSM/I scattering, SSM/I emission, Outgoing Longwave Radiation Precipitation Index (OPI), Geostationary Operational Environmental Satellite (GOES) precipitation Index (GPI), and Microwave Sounding Unit (MSU). Additionally, the enhanced version of CMAP considered here also includes blended NCEP/NCAR reanalysis precipitation values.

Finally, rainfall and evaporation observations were obtained from the Hamburg ocean atmosphere parameters and fluxes from satellite data (HOAPS) version 3.2 monthly dataset, provided at 0.5° resolution from 1987 to 2008. In HOAPS, precipitation and evaporation are derived from SSM/I radiometers observation over the ice-free global ocean. The evaporation is based on the coupled

ocean–atmosphere response experiment (COARE) bulk flux algorithm. The precipitation is based on a neural net approach, trained with a data set of assimilated SSM/I brightness temperatures and the corresponding precipitation values of the ECMWF model (for details, see Andersson et al. 2010).

Despite the critical importance of satellite observations for atmospheric sciences, these datasets are limited in duration (particularly for climate studies), they often lack global coverage (e.g. *W* and *E* are only available over the oceans), and they are affected by significant uncertainties in the algorithms used for converting radiometric measurements, frequently leading to significant differences amongst different satellite-based estimates (e.g. Gutowski et al. 2003; Sohn et al. 2010; Kidd et al. 2012; Gehne et al. 2016). Reanalysis products, aim to fill the gaps through the assimilation of observations to comprehensive global physically based models of the climate system. The drawback of model-based products is that they reflect the systematic errors of the global circulation models (GCMs) used to provide the forecast background (e.g. Trenberth et al. 2011; Lorenz and Kuntzmann 2012; Gehne et al. 2016; Bosilovich et al. 2017). In the present investigation, three different reanalysis products are considered, all of them spanning for more than 100 years with global coverage, hence appropriate for climate variability studies. Additionally, a similarly long run simulation, but without assimilation of observations, is also considered.

The European Centre for Medium Range Weather Forecasts (ECMWF) twentieth century reanalysis (ERA-20C, Poli et al. 2016) provides a long (1900–2010), gap-free gridded record of many climate variables. It uses ECMWF Integrated Forecasting System (IFS) atmospheric global circulation model (cycle Cy38r1), assimilating marine surface winds from the International Comprehensive Ocean–Atmosphere Data Set version 2.5.1 (ICODSv2.5.1) and surface and mean-sea-level pressure from the International Surface Pressure Databank version 3.2.6 (ISPDv3.2.6) and from ICODESv2.5.1. The assimilation methodology is applied from the beginning of the twentieth-century using a 24-h 4D-Var analysis. It also includes prescribed sea surface temperature (*SST*) forcing at monthly time scales from the Hadley Centre Sea Ice and Sea Surface Temperature data set version 2.1. (HadISST2.1). The numerical simulation has 91 vertical levels between the surface and 0.01 hPa with approximately 1° horizontal resolution. Poli et al. (2016) showed that the water cycle in ERA-20C features stable *P–E* global averages and no spurious jumps or trends. Also, they have reported a fair ability of this reanalysis to represent the observed interannual fluctuations of precipitation over land, although with distinct performances between the beginning and end-of-century. Furthermore, when compared to previous reanalysis products, ERA-20C represented an

improvement in the W anomalies compared to satellite data. All ERA-20C fields considered here were obtained at 6-h temporal resolution. Precipitation and evaporation were obtained directly from forecasts, where observations are only included in the initial conditions. The forecasts are integrated daily from 06 UTC. Precipitable water and surface temperature were obtained from assimilated products. Here the surface temperature was obtained by compositing the SST over the oceans with 2-m temperature (T_{2m}) over land, mimicking the procedure used to build the HadCRUT dataset.

ERA-20CM (Hersbach et al. 2015) is a companion product of ERA-20C, providing an AMIP-like ensemble of simulations using the same model, initial conditions, radiative and aerosol forcings and lower boundary conditions. The main differences are that no observations are assimilated and the simulation is integrated continuously over the full 1900–2010 period, in contrast to ERA-20C which is integrated over daily analysis cycles. Here only the control member of the ERA-20CM ensemble is considered and the data was obtained as monthly means of daily means, since daily (or sub-daily) resolution was not available at the ECWMF website for all the required variables. ERA-20CM is meant to provide a statistical estimate of the climate evolution and a good description of the low-frequency variability of the atmosphere during the twentieth century.

Another companion product is the ECMWF coupled climate reanalysis of the twentieth century (CERA-20C). This is a 10-member ensemble reanalysis covering the 1901–2010 period, based on ECMWF's CERA data assimilation system (Laloyaux et al. 2016). It is produced with IFS version Cy41r2, with the same forcings as the ERA-20C and ERA-20CM products. It assimilates the same surface pressure and marine wind observations as ERA-20C, but also profiles of ocean temperature and salinity. The air–sea interface is relaxed towards the SST from HadISST2.1 to avoid model drift while enabling the simulation of coupled processes.

Finally, the National Oceanic and Atmospheric Administration Cooperative Institute for Research in Environmental Sciences (NOAA-CIRES) twentieth century reanalysis (20CR) version 2c (Compo et al. 2011) was also considered. It covers the full globe at 2° resolution, spanning from 1851 to 2014. The 20CR variables considered here were obtained at daily resolution for the 1900–2010 period. 20CR uses the National Centers for Environmental Prediction (NCEP) Global Forecast System (GFS) along with an Ensemble Kalman Filter data assimilation technique (Whitaker and Hamill 2002). It assimilates only surface pressure observations and reports. SST boundary conditions are obtained from 18 members of pentad Simple Ocean Data Assimilation with Sparse Input (SODAsi) version 2, with the high latitudes corrected to the centennial in situ observation-based estimates of the variability of SST and marine meteorological variables, version 2 (COBE-SST2).

The main characteristics of the datasets considered in the present investigation are summarized in Table 1. Rather than focusing on the limitations and uncertainties associated with each individual product, the present study takes advantage of the availability of several climate databases of different origins to evaluate the robustness of the multi-scale structure revealed by spectral and DCCA analysis.

2.2 Detrended cross-correlation analysis

In a temporal scaling regime, the fluctuations of a given time-series F display a power-law dependence on time-scale $\Delta F(\Delta t) \approx \Delta t^H$, where H is a scaling exponent, and $\langle \rangle$ indicates statistical averaging. It is traditional (and often sufficient) to define the fluctuations by absolute differences: $\Delta F(\Delta t) = |F(t + \Delta t) - F(t)|$. However, this definition is only adequate for fluctuations increasing with time-scale (i.e. $H > 0$), but it does not estimate the fluctuations correctly when fluctuations decrease with time-scale (i.e. $H < 0$) (Lovejoy and Schertzer 2013). As will be seen in Sect. 3.1, the atmospheric time-series considered here display a $H < 0$

Table 1 Summary of the main characteristics of the climate datasets considered in the present investigation

Product	Data type	Variables	Period covered	Temporal resolution	Spatial resolution
ERA-20C	Reanalysis (uncoupled)	T_s, P, E, W	1900–2010	6 h	$1^\circ \times 1^\circ$
ERA-20CM	GCM (uncoupled)	T_s, P, E, W	1900–2010	Monthly	$1^\circ \times 1^\circ$
CERA-20C	Reanalysis (coupled)	T_s, P, E, W	1901–2010	Monthly	$1^\circ \times 1^\circ$
20CR	Reanalysis (coupled)	T_s, P, E, W	1851–2012	Daily	$2^\circ \times 2^\circ$
HadCRUT	Satellite/station hybrid	T_s	1850–present	Monthly	$5^\circ \times 5^\circ$
GISSTEMP	Satellite/station hybrid	T_s	1880–present	Monthly	$2^\circ \times 2^\circ$
RSS	Satellite based	W	1988–present	Monthly	$1^\circ \times 1^\circ$
GPCP	Satellite/station hybrid	P	1979–present	Monthly	$2.5^\circ \times 2.5^\circ$
CMAP	Satellite/station hybrid	P	1979–present	Monthly	$2.5^\circ \times 2.5^\circ$
HOAPS	Satellite/model hybrid	P, E	1987–2008	Monthly	$0.5^\circ \times 0.5^\circ$

regime at time-scales larger than a few months. Thus, simple mean absolute differences are not appropriate for the present purpose, and detrended cross correlation analysis (DCCA) was used instead. DCCA was first proposed by Podobnik and Stanley (2008) to accurately quantify power-law correlations between two different time-series over wide ranges of time-scales. It is based on detrended fluctuation analysis (DFA), which has been shown to accurately quantify the fluctuations in the $-1 < H < 1$ range (Lovejoy and Schertzer 2013). Notice that other methods could be used to estimate fluctuations in both positive and negative H cases, such as the often used “Haar fluctuations” (Lovejoy and Schertzer 2013; Lovejoy 2015; Lovejoy et al. 2017; De Lima and Lovejoy 2015).

Consider two time-series, y and y' , with N data points each. Due to the strong yearly cycle present in the time-series considered here, a preliminary step is required prior to employing DFA analysis: following Kantehardt et al. (2002), the periodic seasonal trend is eliminated by subtracting the long-term average (over all the years in the record) of each calendar day (or each month, for monthly time-series):

$$y_{ds}(i) = y(i) - \langle y \rangle_d, \tag{3}$$

where y_d denotes the climatological average value for the given calendar day (or month). This is repeated for both y and y' . Notice that daily time-series are used for DCCA analysis from ERA-20C time-series, thus removing the daily periodic signal. All other datasets have daily or coarser resolutions. Subsequently, two integrated signals, R and R' , are constructed from the deseasonalized time-series using Eq. 4:

$$R_k = \sum_{i=1}^k [y_{ds}(i) - \langle y \rangle_{ds}], \tag{4}$$

where $k = 1, \dots, N$ and y_{ds} is the mean of the deseasonalized time-series. The integrated signals are divided into $N - n$ overlapping segments, each containing $n + 1$ values. The time-lagged correlations can be obtained by computing $R_{k+\tau} = \sum_{i=1}^k [y_{ds}(i) - y_{ds}]$ with $k + \tau = 1, \dots, N$ (for details, see Chenhua 2015). For each segment from each integrated signal, the “local trend” is estimated using a first-order polynomial. The detrended integrated signal is then defined as the difference between the original integrated signal and the local trend $(R_v - \tilde{R}_v)$, where \tilde{R}_v is the fitting first-order polynomial to the v th segment R_v . Next, the covariance of the residuals in each segment is calculated as:

$$f_{R,R'}^2(n, i) = \frac{1}{n + 1} \sum_{k=i}^{i+n} [(R_v - \tilde{R}_v)(R'_v - \tilde{R}'_v)], \tag{5}$$

The detrended covariance is estimated by summing over all overlapping $N-n$ segments:

$$F_{R,R'}^2(n) = \frac{1}{N - n} \sum_{i=1}^{N-n} f_{R,R'}^2(n, i), \tag{6}$$

Finally, the DCCA cross-correlation coefficient at time-scale n , $\rho_{DCCA}(n)$, are defined as the ratio between the detrended covariance function and the product of the square-rooted detrended variance function for each time-series:

$$\rho_{DCCA}(n) = \frac{F_{R,R'}^2(n)}{\sqrt{F_{R,R}^2(n)} \times \sqrt{F_{R',R'}^2(n)}}, \tag{7}$$

The value of $\rho_{DCCA}(n)$ is in the $[-1, 1]$ range and can be computed for different time-scales. DCCA has been previously demonstrated to accurately quantify power law scale-dependent cross-correlations between different simultaneously recorded time-series (Podbnik and Stanley 2008; Horvatic et al. 2011; Piao and Fu 2016). Podobnik et al. (2011) have shown that critical points for the 95% significance level of ρ_{DCCA} can vary between values below 0.1 and up to about 0.4, dependent on the time series length, the considered time-scale, and the power law exponents of both time-series. Here it is assumed that ρ_{DCCA} values below 0.3 are nonsignificant, and that ρ_{DCCA} values in the 0.3–0.4 range should be interpreted with care.

2.3 Spectral analysis

The Fourier spectral analysis is an alternative way to investigate the presence of scaling behavior over wide ranges of time-scales, manifested as log–log linearity of the power spectrum, $E(f)$:

$$E(f) \propto f^{-\beta}, \tag{8}$$

where f represents frequency and β is the spectral scaling exponent. Spectral analysis has the advantage of representing a simple framework, often familiar to atmospheric scientists, and is quite sensitive not only to the presence of scaling behavior but also to scaling breaks and other types of deformation of the power–law behavior. Here the intermittency correction is neglected as a simplification, corresponding to the case where the fluctuations are quasi-Gaussian. This approximation generally applies to atmospheric fields at time-scales between a few months and a about a decade (Lovejoy 2015; de Lima and Lovejoy 2015; Lovejoy et al. 2017), where the spectral exponents were estimated in the present study. Under this approximation, β is trivially related to H by the following equation (e.g. Lovejoy and Schertzer 2013):

$$\beta = 1 + 2H, \tag{9}$$

Equation 9 states that for the case where the mean fluctuations increase with time-scale, i.e. a statistically

nonstationary process with $H > 0$, the spectral exponent is $\beta > 1$. On the other hand, for the case where the mean fluctuations decrease with time-scale, i.e. a statistically stationary process with $H < 0$, the spectral exponent is $\beta < 1$.

Here the global spectrum was computed by ensemble averaging over all individual spectra from each grid point, hence considering that each grid point time-series corresponds to a different realization of the same stochastic process, as is the common procedure in scaling analysis of atmospheric fields (see e.g. Lovejoy and Schertzer 2013; Fredriksen and Rypdal 2016). The spectral exponent is estimated by a linear fit to the log–log power spectrum. To more uniformly weight the estimate and reduce noise, spectra are binned into uniform log-frequency intervals and averaged prior to fitting β , as commonly done in this type of analysis (e.g., Huybers and Curry 2006; Lovejoy and Schertzer 2013; Fredriksen and Rypdal 2016). Furthermore, the frequencies around the annual period and the respective harmonics are removed prior to the log-binning by excluding an adequate length frequency window around each peak, following Huybers and Curry (2006). This step ensures that the effect of these high-amplitude isolated peaks does not affect the β estimation. A preliminary analysis showed that the different spatial and temporal resolutions of the datasets considered here (see Table 1) have no impact on the global-scale DCCA and spectral analysis presented in Sect. 3. None of the results and conclusions presented in the present manuscript were changed by first interpolating the datasets to coarser resolutions, before the multiscale analysis was employed. Thus, the original resolution of the datasets was preserved to avoid the further complications and spurious artifacts introduced by spatial interpolation techniques.

3 Results

3.1 Spectral analysis

The global-mean spectra of T_s , W , P and E display significant variability over a wide range of temporal scales, superposed on the high-amplitude peaks of the yearly and daily periodic signals (Fig. 1). Notice that the HadCRUT4 and GISSTEMP time-series represent anomalies, thus representing deseasonalized time-series. Consequently, their respective spectra in Fig. 1a show highly smoothed yearly peaks. An important feature that is present for both higher temporal resolution datasets (ERA-20C and 20CR) in all the considered variables is a clear transition between steeper slopes at short time-scales (below about 10 days) and a much flatter region at longer time-scales. The (curved) transition scale range in the global-averaged T_s spectrum (Fig. 1a) extends between about 10 days and 3 months, much wider than the more abrupt transitions in W (Fig. 1b) and E (Fig. 1d)

spectra occurring around 10 days. For the P spectrum (Fig. 1b), the change in the slopes is less pronounced (particularly for ERA-20C), but the transition is still present, occurring at time-scales around 10 days. As discussed in Lovejoy (2015), this ubiquitous transition separates a high-frequency weather regime that extends up to about the synoptic time-scales (~ 10 days), from a low-frequency weather regime (often denoted by macroweather) that extends up to a few decades. The dashed-dotted lines in Fig. 1 show that the weather regime for T_s , W and E are characterized by $\beta > 1$, i.e. statistically non-stationary behavior, and thus the fluctuations tend to increase with increasing time-scale. For P spectra, β is closer to 1, being slightly below in ERA-20C and slightly above for 20CR. A time-series with $\beta \approx 1$ will maintain the amplitude of its fluctuations as time-scale increases. For the macroweather regime, $\beta < 1$ values are found for all time-series, i.e. statistically stationary behavior, and thus the amplitude of the fluctuations tends to decrease with increasing time-scale, hence implying a convergence toward the ‘climate normal’ at time-scales of a few decades. Notice that β cannot be robustly quantified here for the weather regime given the very short range of scales available for this regime in both ERA-20C and 20CR datasets, made worse by the presence of strong diurnal peaks in ERA-20C.

Another transition has been reported at time-scales larger than a few decades, where the climate regime emerges, and fluctuations tend to grow with increasing time-scale (i.e. $\beta > 1$). Figure 1 shows some hints of this transition at multi-decadal time-scales, although there is considerable disagreement between datasets on the position and magnitude of this transition. For example, there is a transition to steeper slopes in the global T_s spectra (Fig. 1a) in all datasets except HadCRUT4. P and E spectra (Fig. 1c, d respectively) also suggest a similar transition in ERA-20C, CERA-20C and 20CR, but not in ERA-20CM. In contrast, the transition to the climate regime in global W spectra (Fig. 1b) is less pronounced or inexistent at time-scales up to about 50 years. However, it is important to notice that due to the limited length of the considered datasets the spectral resolution at these large time-scales is very low and the results should be interpreted with care.

The macroweather spectral slopes were quantified for ERA-20C and 20CR (see Table 2). Both datasets have a large amount of data-points over the macroweather scale range, thus allowing a robust (log–log) linear regression. Overall, 20CR reanalysis showed slightly larger β values than ERA-20C, although the differences are mostly within the typical 0.1–0.2 error margin in β estimation (see e.g. Barros et al. 2004; Nogueira and Barros 2015). The spectral slopes associated with global-averaged T_s and W in the macroweather are slightly larger than for P and E , but again the differences are within the 0.1–0.2 margin. The spectral slopes for the other datasets were not estimated directly due

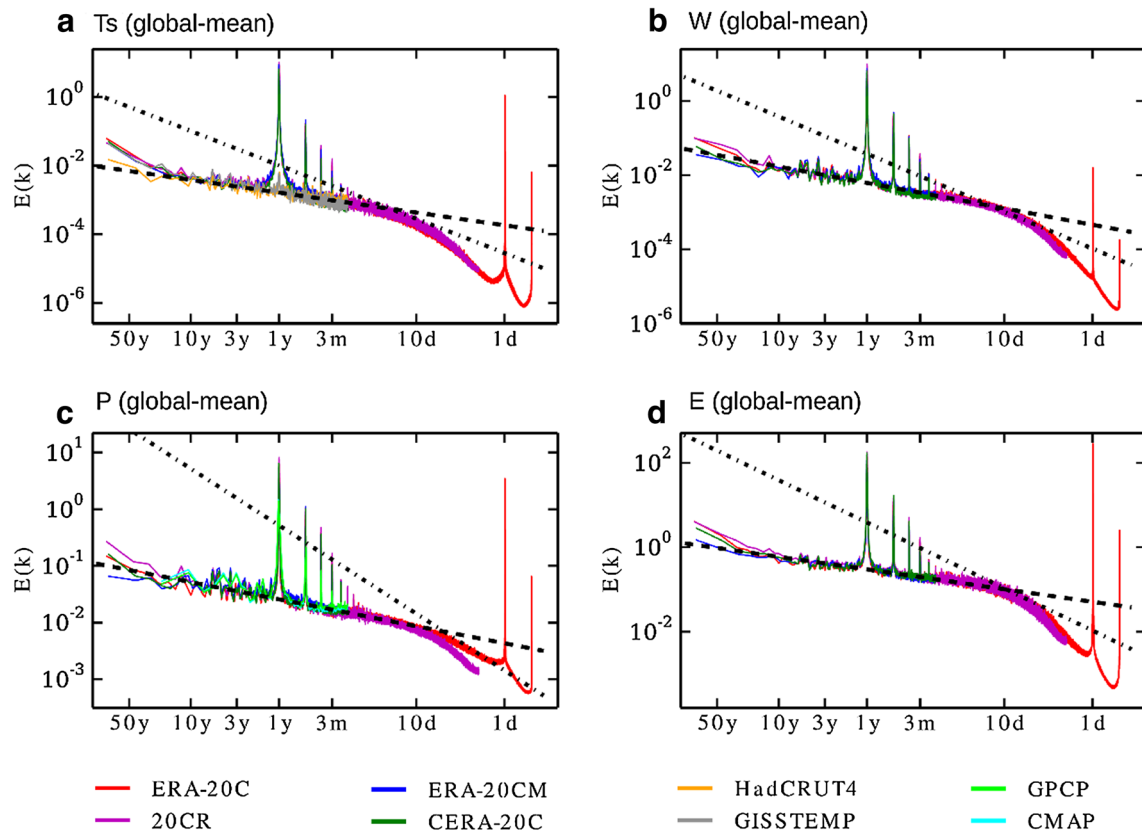


Fig. 1 Power spectra in log–log axis computed from the different model-based and satellite-based datasets for global-mean time-series of **a** T_s , **b** W , **c** P and **d** E . The black dashed line represents the esti-

ated spectral exponent averaged between ERA-20C and 20CR (see Table 1). The black dashed–dotted line represents $\beta = 1$

to short length of these monthly time-series resulting in coarse spectral resolution, particularly at the larger temporal scales (specially for the satellite based products restricted to the last four decades or so). Nonetheless, visual inspection of Fig. 1 shows that β obtained by averaging the spectral slopes from ERA-20C and 20CR fits to a good approximation the respective global-mean spectra of T_s , W , E and P from all other datasets, for a scale range extending from about 3 months to about a decade. In fact, the results show an overall good agreement of the slopes in the macroweather scale range amongst the different datasets. Notice that the agreement is somewhat degraded at scales larger than about 10 years. But a rigorous analysis of such large time-scales

is not possible due to the limited length of the time-series (at most ~ 110 years), and these differences should be interpreted with care.

The main features of the global-mean spectra of T_s , W , P and E spectra are also present in the spectra computed separately over the global ocean (Fig. 2) and global land (Fig. 3): the significant variability across the considered range of scales superposed on the periodic peaks (yearly, daily and respective harmonics), the weather-to-macroweather regime transition with flatter slopes ($\beta < 1$) in the latter, and the generally good agreement of the common (3-monthly to decadal) portion of the spectra between all the considered datasets (model based and observational) for all the considered

Table 2 Spectral exponents estimated for T_s , W , P and E time-series from ERA-20C and 20CR data, averaged over the full globe, global ocean and global land

	Global			Ocean			Land		
	ERA-20C	20CR	Avg	ERA-20C	20CR	Avg	ERA-20C	20CR	Avg
T_s	0.35	0.39	0.37	0.51	0.55	0.53	0.24	0.29	0.27
W	0.40	0.48	0.44	0.43	0.51	0.47	0.27	0.40	0.34
P	0.26	0.34	0.30	0.27	0.36	0.32	0.17	0.27	0.22
E	0.27	0.33	0.30	0.25	0.31	0.28	0.32	0.50	0.41

The β values averaged between both datasets are also presented

variables. An interesting difference between land and ocean spectra is the weather-to-macroweather transition time-scale for T_s , which is ~ 1 month over land (Fig. 3a), and much closer to 1 year over the oceans (Fig. 2a). This difference is in agreement with Lovejoy (2015) predictions: the higher (lower) magnitude turbulent fluxes associated with the atmosphere (ocean) result in a shorter (longer) time-scale of transition between weather and macroweather, occurring around 10 days (1 year).

The land spectra show a somewhat weaker agreement amongst different datasets (Fig. 3). Specifically, ERA-20CM displays slightly flatter macroweather spectra compared to the other datasets for all considered variables, although these differences are more pronounced at scales larger than about 10 years, for which the analysis of the spectrum is not robust. Another notorious feature is a fast drop in HOAPS E variability at scales below about 1 year, which should be a spurious artifact of this dataset given its abruptness compared to all variables in all other datasets.

Table 2 shows that β values for T_s spectra over the global ocean are steeper (~ 0.5 – 0.6) compared to global land (~ 0.2 – 0.3) or to the full globe (~ 0.4). Previously, Nogueira (2017b) showed that SST in reanalysis products displays spurious abrupt drop in variability at time-scales below a few

months over vast regions of the globe due to the monthly resolution of the forcing dataset. This fact could explain the steeper oceanic slopes obtained here. Nonetheless, the steeper slopes found here for reanalysis products agree with the observational dataset spectra (HadCRUT and GISSTEMP) and may have a physical basis, associated with the presence of stronger forcings (and variability) at larger time-scales over the oceans, due to the longer time-scales associated with oceanic processes compared to land. Furthermore, several previous studies have reported significant variation of the temperature macroweather scaling exponents between oceans and land, although with significant spread amongst the exact quantitative estimates depending on the particular methodology and dataset, but corresponding to $\beta < 1$ in all cases (see Lovejoy 2015 for a review and discussion). The W and P spectral exponents are also slightly larger over oceans compared to land, but only by about 0.1. Notice that the estimates of the P spectral slopes in Table 2 are close to the estimates by de Lima and Lovejoy (2015) of $\beta \sim 0.2$ for ocean, land and full globe obtained using a different technique to estimate the scaling exponents from three datasets (20CR, a different satellite-based product and a gridded station-based product). For evaporation, the spectral exponents are slightly larger over land (~ 0.3 – 0.5) than over the

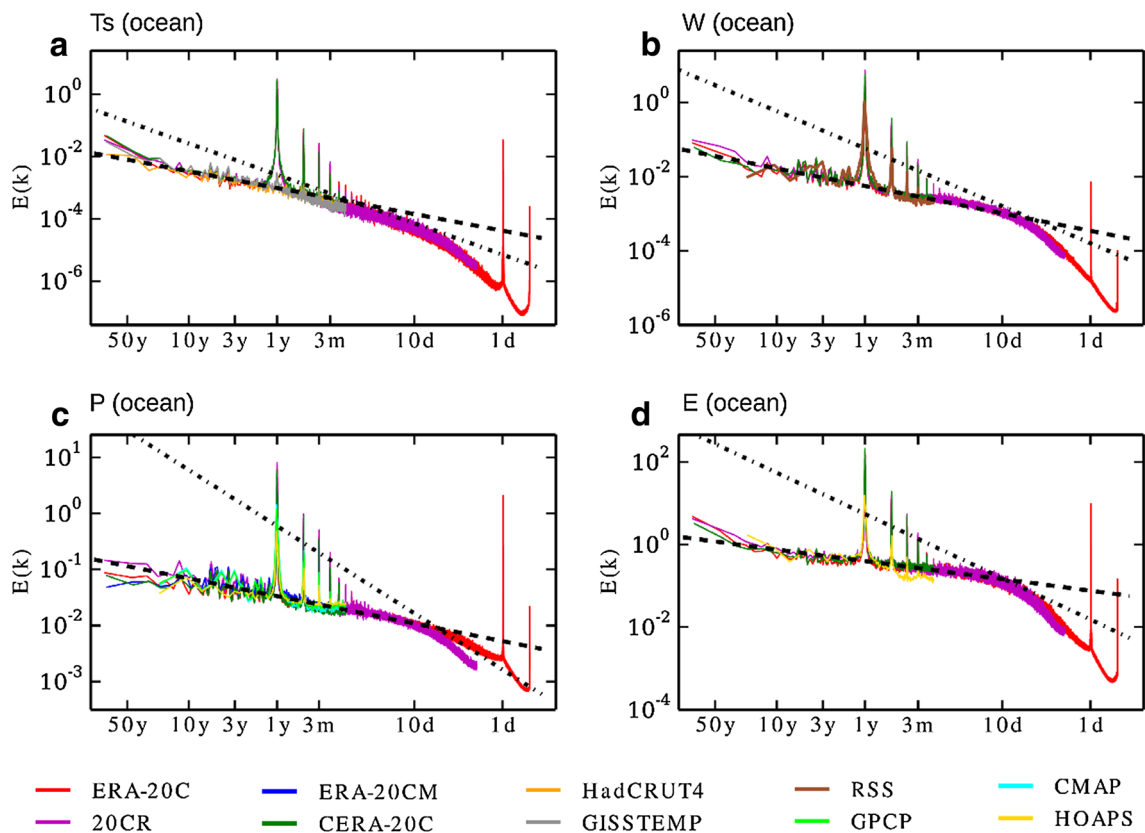


Fig. 2 Same as Fig. 1 but the spectra are computed for global ocean only

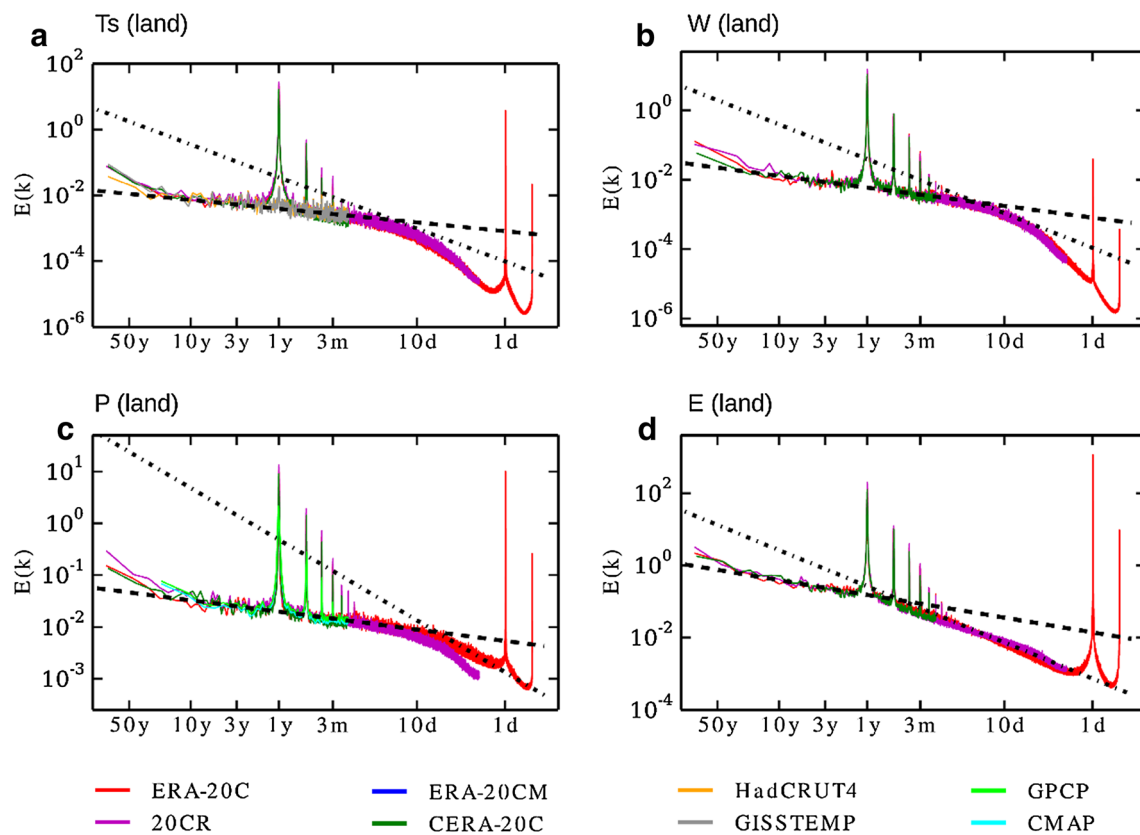


Fig. 3 Same as Fig. 1 but the spectra are computed for global land only

ocean (~ 0.2 – 0.3). Additionally, for E over land the transition between flatter large-scales and steeper small-scales seems to occur at higher time-scales (close to 1 year). This behavior reflects the complex land–atmosphere interactions, including the limited moisture availability over land in contrast to the infinite oceanic source. However, a detailed analysis of this behavior is beyond the scope of the present manuscript.

3.2 DCCA

In the present section, DCCA is employed to study how the complex variability structure found in the previous section for large-scale W , P and E may be related to the complex variability of T_s time-series, taking into consideration the C–C relationship. Figure 4 shows ρ_{DCCA} at lag-zero for time-scales between 5 days and 9 years. The non-periodic component of global-mean W and T_s time-series are very tightly correlated ($\rho_{DCCA} \sim 0.9$) at time-scales larger than about 3 years (Fig. 4a, b), in tight agreement with the C–C relationship. However, ρ_{DCCA} decreases rapidly for shorter time-scales and negligible correlations are found at time-scales below about 6 months. Similar transitional behavior is found for W vs T_s across all model based datasets for full globe averages, but also when considering the global

oceans (Fig. 5a, b) or global land (Fig. 6a, b) separately. Additionally, similar transitional behavior is also found for RSS against GISTEMP or HadCRUT (Fig. 5a). The results also show that the high correlations between W and T_s at large-temporal scales are stronger over the ocean (nearly 0.9) compared to land, particularly for ERA-20CM and CERA-20C where maximum correlations over land decrease to about 0.7. Interestingly, Lovejoy et al. (2017) reported a similar transitional behavior for the correlation between air temperature over land and over the ocean. They suggested that high correlations at multi-year time-scales corresponds to strong atmosphere/ocean coupling, while the low correlations at shorter time-scales corresponds to an uncoupling of atmospheric and ocean variability.

The multi-scale correlation structure of global-mean P against T_s shows a larger spread amongst different datasets (Fig. 4c, d). The products based on ECMWF model (ERA-20C, ERA-20CM and CERA-20C) show an increase in ρ_{DCCA} , from negligible values at time-scales below a few months to values between 0.7 and 0.8 at time-scales larger than a few years, analogous to the behavior found for W against T_s . 20CR reanalysis shows a slower increase of ρ_{DCCA} , which reaches lower maximum correlation values (slightly below 0.6). The increase is even slower for GPCP

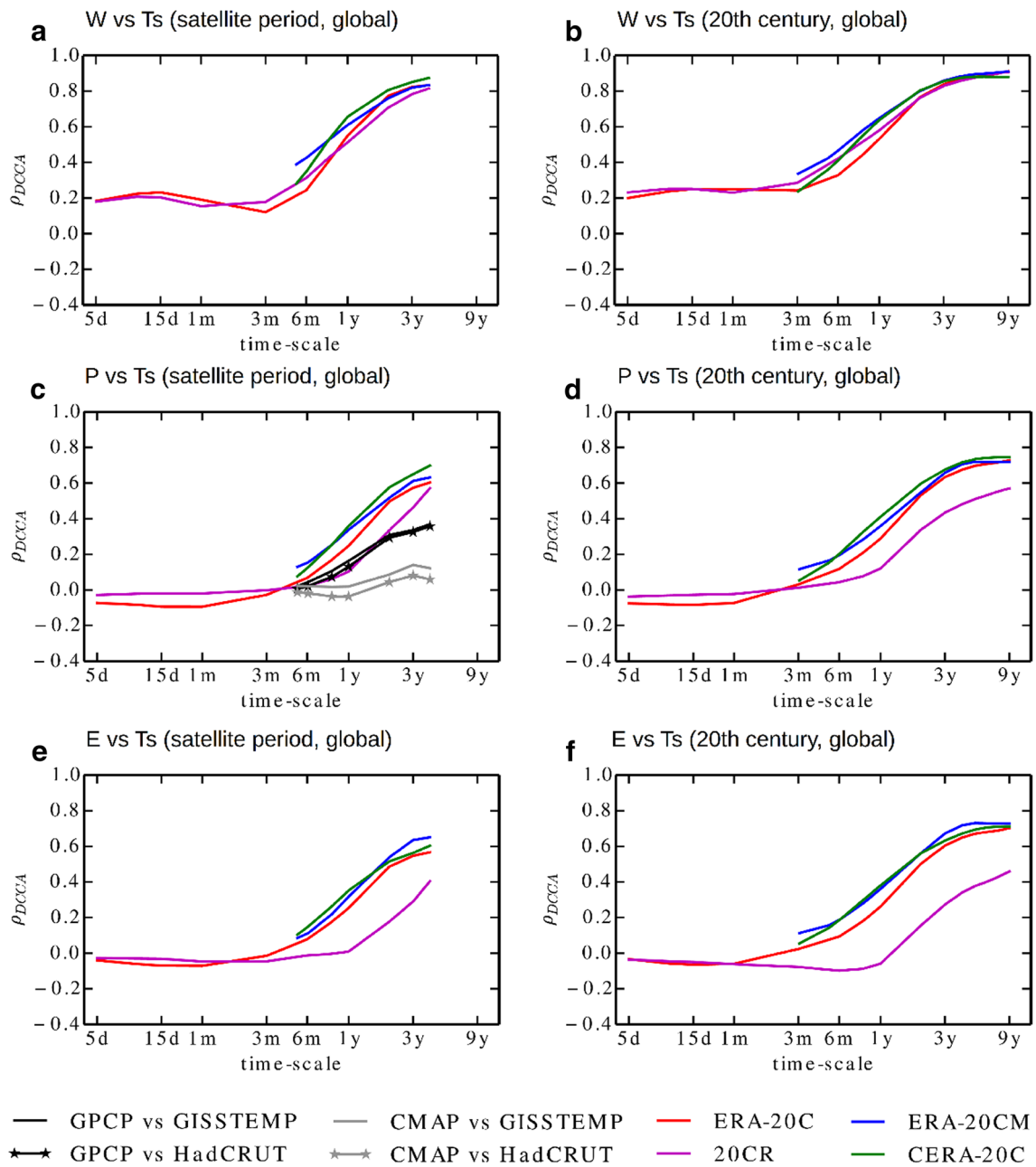


Fig. 4 DCCA cross-correlation coefficients against temporal scale computed for global-mean time-series of **a, b** W vs T_s ; **c, d** P vs T_s ; and **e, f** E vs T_s . In the left column only the 1979–2016 is considered

(or sub-sets of this period depending on the particular dataset record length), while in the right column the full 1900–2010 period is considered (1901–2010 for CERA-20C)

against HadCRU or GISSTEMP, from nearly zero correlations at scales of a few months to only ~ 0.4 at 3–4 years. Finally, CMAP shows $\rho_{DCCA} < 0.2$ (negligible) for all the considered time-scales. Hence there is significant discrepancy between different climate models and even larger when satellite-based products are considered. These differences range from a good agreement with the C–C scaling of precipitation at scales larger than a few years to no significant correlations at these same temporal scales. It is important to

notice that the fact that correlations are low does not mean that C–C is not important. It might be the case that various forcings may work at different time-scales in controlling the precipitation variability.

The multi-scale correlation structure between global-mean E and T_s in model based products (Fig. 4e, f) is similar to the behavior found for global-mean P and T_s , with ECMWF models showing ρ_{DCCA} varying between nearly zero values at scales below a few months to values > 0.7 at

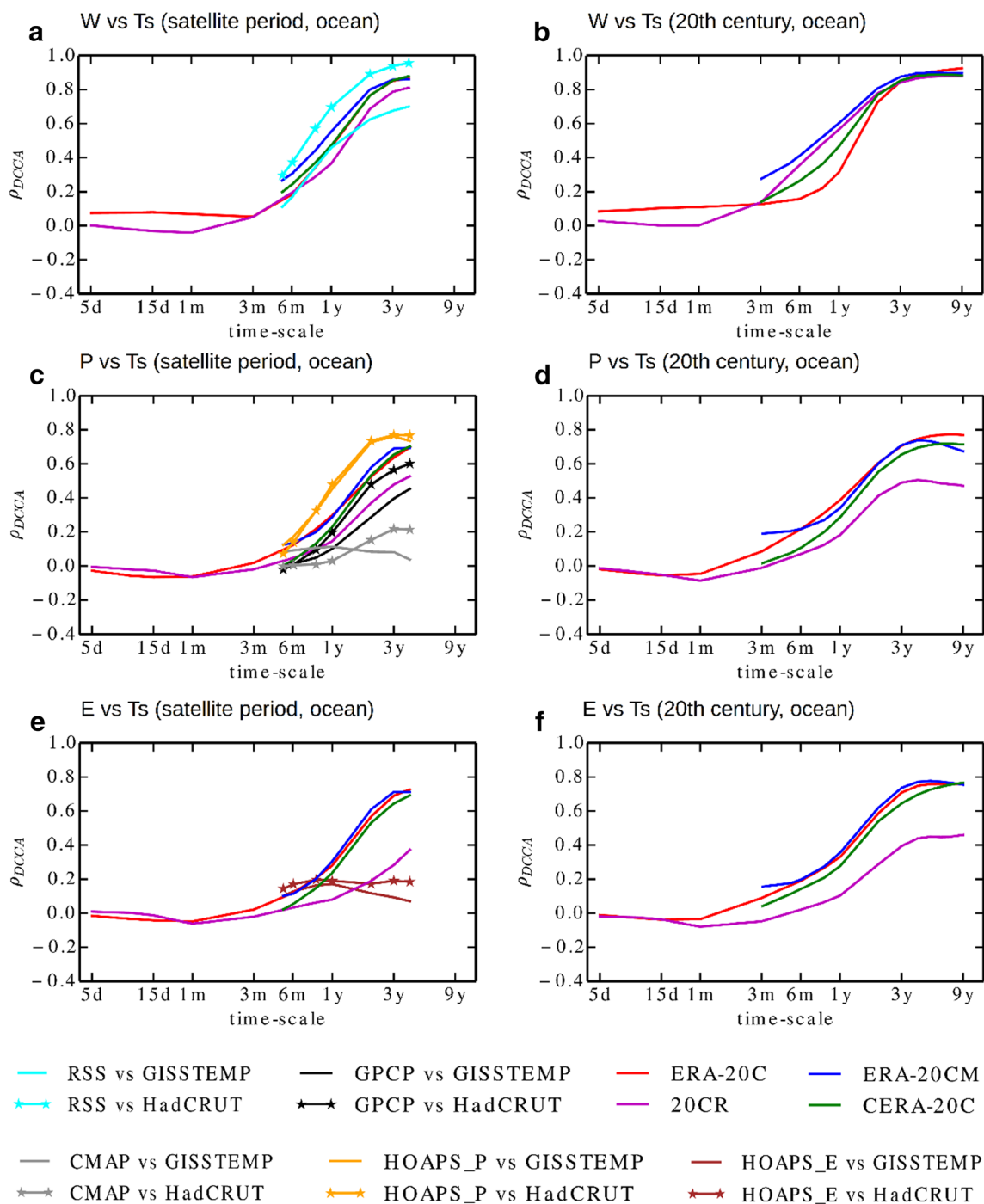


Fig. 5 Same as Fig. 4, but for time-series averaged over global ocean only

scales larger than a few years. 20CR shows a much more modest increase to values only slightly above 0.4 (only marginally significant). No observational products are available for *E* over land, and thus, nor for global scale.

Over the oceans, the correlation of *P* against *T_s* for model products is analogous to what was found for the full globe,

but with larger discrepancy between maximum ρ_{DCCA} in ECMWF models ($\sim 0.7\text{--}0.8$) and 20CR (~ 0.5) at long time-scales. Another relevant difference is the increase in the correlation of GPCP against HadCRUT, reaching values around 0.6 at 3- to 4-year time-scales, after growing significantly from near zero values at time-scales of a few months. The

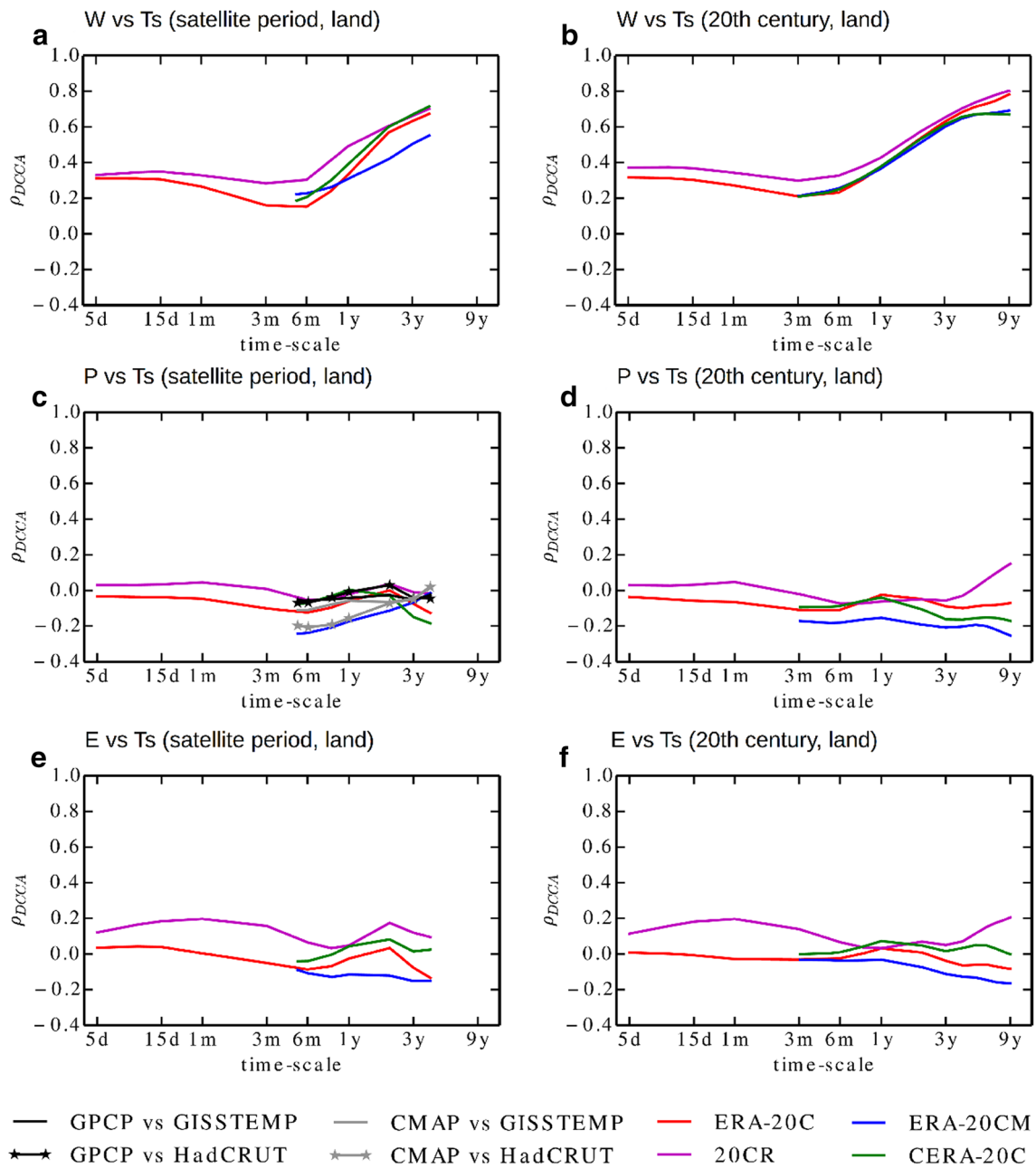


Fig. 6 Same as Fig. 4, but for time-series averaged over global land only

maximum correlation is reduced to around 0.4 for GPCP against GISSTEMP. Again, negligible correlations are obtained when CMAP is considered. Finally, for HOAPS P ρ_{DCCA} grows from nearly zero correlations to values around 0.8, both against HadCRUT and GISSTEMP. Notice, however, that due to the short record length of HOAPS dataset, the high ρ_{DCCA} values found for HOAPS P (Fig. 5c) and low ρ_{DCCA} found for HOAPS E product (Fig. 5e) should be interpreted with care. Nonetheless, the disparity in the multi-scale correlation structure for long-temporal over the oceans

for different datasets is large, ranging from negligible correlations to large ρ_{DCCA} values.

For E against T_s over the ocean the results are nearly identical to the full globe. However, in the former case a satellite-based product is available (HOAPS), which shows negligible correlations at all the considered time-scales, in clear contrast with the ECMWF model based products and slightly lower than the 0.4 maximum correlations in 20CR. However, as pointed out above, the HOAPS E has a short record length. Furthermore, the HOAPS E spectrum in Fig. 2d showed a seemingly spurious variability structures

at scales below about 1-year, which could significantly influence the correlations and hence the results should be interpreted with care. Finally, for time-series averaged over global land, no significant correlations were found between P and T_s , nor between E and T_s for all the available datasets, with all $|\rho_{DCCA}|$ below about 0.2 (Fig. 6c–f).

Notice that the multiscale structure ρ_{DCCA} from model based products, either showing a sharp increase between fast and slow time-scales or a constant negligible correlation across scales does not change when only the analysis is performed only for the satellite period (left column in Figs. 4, 5, 6) or when the full 1900–2010 period is considered (right column in Figs. 4, 5 and 6). Additionally, the use of different reference climatological periods to deseasonalize the time-series (e.g. 1951–1980, 1961–1990 or 1981–2010) produced changes below 0.05 in ρ_{DCCA} estimates (not shown). Furthermore, the differences in ρ_{DCCA} remain below 0.03 when 2-m temperature or land/sea-surface temperatures are used over the full globe instead of their composite (see Sect. 2.1), or when total atmosphere column water (including liquid) is used instead of W (not shown). This consistency of the ρ_{DCCA} multi-scale structure provides further robustness to the present results. Notice also that the similarity between the multi-scale correlation structure for all considered variables between ERA-20C, ERA-20CM and CERA-20C datasets suggest that the data assimilation and the atmosphere–ocean coupling methodologies do not significantly impact the sensitivity of the global water cycle on surface temperature.

3.3 Lagged DCCA

In the previous section, the hypothesis that the correlations of global scale W , P and E against T_s time-series could be lagged was not considered. This is a potential explanation for the sharp decrease in correlations at time-scales below a few years. In fact, Gu and Adler (2011, 2012) did find the maximum correlation-coefficients of similar time-series at inter-annual scale to occur at a few months. This hypothesis is tested in the present section using lagged-DCCA.

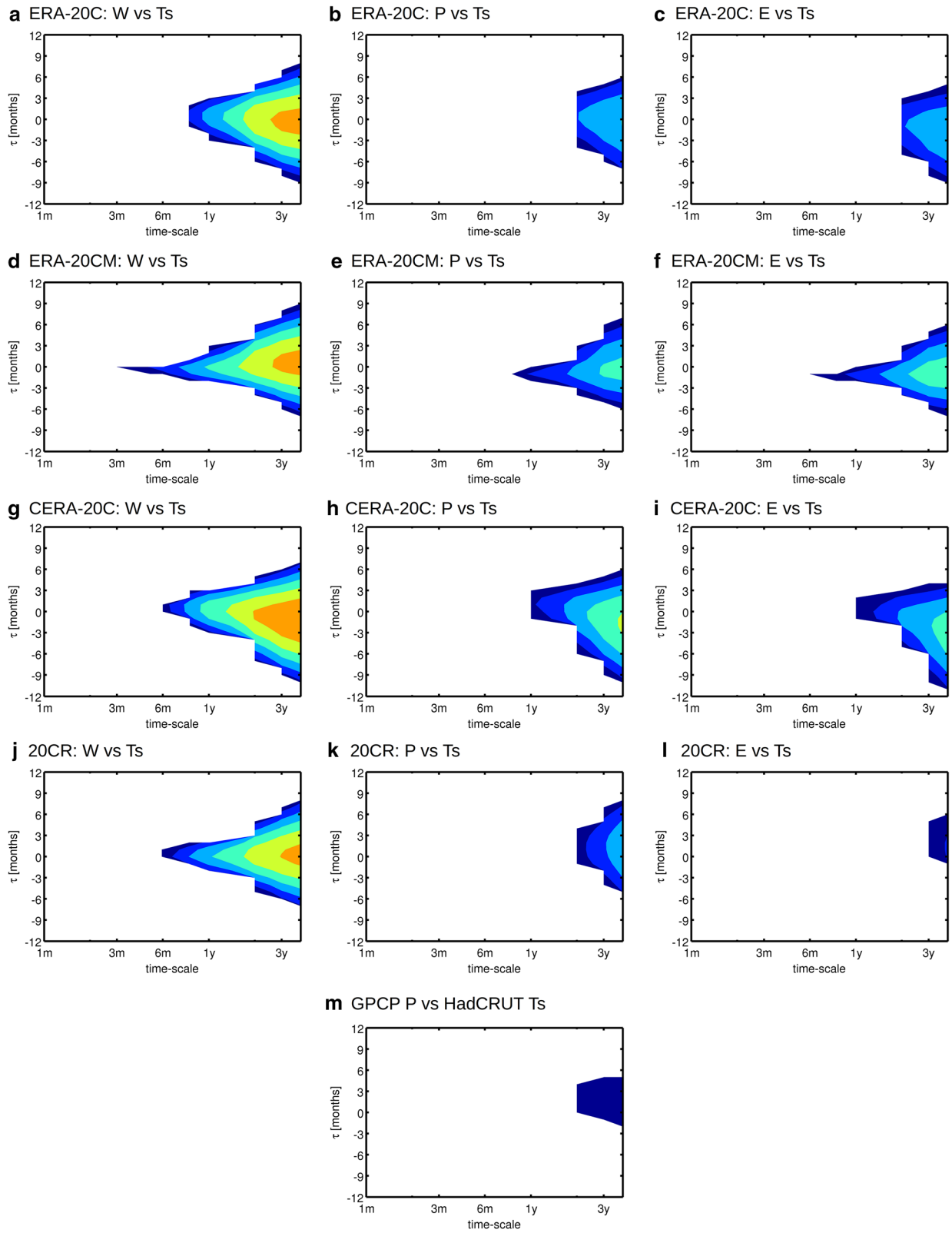
For all model based datasets, the multi-scale correlation structure global-mean W and T_s time-series shows negligible values (<0.3) at time-scales below a few months, regardless of the considered lag (Fig. 7). As the time-scale increases, ρ_{DCCA} increases rapidly with maximum values centered at lags close to zero, reaching values >0.8 for time-scale larger than a few-years. Consequently, the multi-scale correlation structure at lag zero in Fig. 4a, b represents well the correlation structure between global-mean W and T_s . Figures 7, 8 and 9 show that all the main results on the correlations global-mean P or E against T_s time-series at lag zero presented in the previous section are also essentially unchanged by considering the possibility of lagged correlations. Although the actual maximum correlation might occur

at lags of a few months in some cases (e.g. global-mean P against T_s in CERA-20C, Fig. 7j), the differences to the lag-zero are essentially within 0.1. It is important to notice that when the lag τ is lower than the temporal resolution considered (i.e. n in Eq. 5), the lagged-DCCA method effectively overlaps a portion of the statistical information, which can obscure the results. Nonetheless, the present results confirm that the negligible correlations between P , E or W against T_s at time-scales below a few months is robust, even when a lag is considered. Furthermore, the presence of a transition to very high-correlations as the time-scale increases to multi-year time-scales is also robust, although the exact lag at which the maximum correlation occurs cannot be exactly determined by this methodology.

3.4 Sensitivity coefficient estimation

The sensitivity coefficient of precipitable water to surface temperature was estimated by linear regression following Eq. 2. The results presented in Table 3 were obtained by considering fluctuations of coarse-grained 3-yearly averaged time-series, after removing the respective linear trends. The 3-year time-scale is chosen as representative of the longer-scale high-correlation regime, while maximizing the number of data-points. The α values for cases where ρ_{DCCA} is considered non-significant or unreliable (i.e. $\rho_{DCCA} < 0.4$) are neglected (not computed). At the global-mean scale, W shows sensitivities in the 7–10%/K range, slightly above the typical 7%/K derived from the C–C relationship. The estimated values are somewhat larger over the oceans (7–11%/K) than over land (4–7%/K). The RSS vs GISTEMP shows the lowest sensitivity over the ocean (7%/K). This is also the dataset with the lowest regression coefficient, $r^2 = 0.47$ compared with r^2 values in the 0.72–0.91 range for all other datasets. It also corresponds to the lowest ρ_{DCCA} value in Fig. 5a. Hence, this value may be neglected, and the α range for the ocean becomes 9–11%/K. Although the results over ocean, land and full globe can differ slightly from the theoretical 7%/K, they agree with previous estimates of precipitable water sensitivity at global scales (see e.g. Schneider et al. 2010 for a review).

The sensitivity coefficients of global-mean P and E against T_s are both in the 3–4%/K range (with r^2 in the 0.45–0.62 range), which is close to the often reported 1–3%/K. Over the ocean, the sensitivity of P to T_s fluctuations display spreads over a wider range of values, 4–11%/K, which can be much larger than the typical 1–3%/K values. On the one hand, other previous works have also found larger precipitation sensitivities (over 6%/K) (e.g. Wentz et al. 2007). On the other hand, the α estimates have been shown to be highly sensitive to the length of the record used and spatial domain considered (Gu and Adler 2013; Adler et al. 2017). In fact, our results over the ocean show large



ρ_{DCCA} 0.3 0.4 0.5 0.6 0.7 0.8 0.9 1

Fig. 7 DCCA lagged cross-correlation coefficients (color scale) as a function of temporal scale and temporal lag, τ computed for global-mean time-series of W vs T_s (leftmost column); P vs T_s (center column); and E vs T_s (rightmost column). Non-significant $\rho_{DCCA} < 0.3$ values are not shown. Only datasets where significant correlation values exist are shown, except for GPCP vs GISSTEMP which is nearly identical to GPCP vs HadCRUT in panel n

dispersion amongst datasets and low r^2 values for the linear regressions, in the 0.10–0.65 range, being lowest for HOAPS P products which show the highest α values and have the shortest record length (1988–2008). In fact, neglecting the HOAPS P dataset, the sensitivity of P to T_s is in the range of 4–7%/K. This range is close to the 3–6%/K values found for the sensitivity of E to T_s over the ocean (with r^2 in the 0.65–0.66), and closer to the more typical 1–3%/K.

Finally, there are no significant correlations between P and T_s or E and T_s over land at none of the considered time-scales, i.e. C–C is not a dominant mechanism of P or E variability over land, and thus α was not computed.

4 Summary and discussion

The components of the atmospheric branch of the global water cycle (precipitable water, precipitation and evaporation) and near surface temperature showed significant variability over a wide range of time-scales (spanning from a few days up to a few decades), superposed on high amplitude daily and yearly periodic peaks. As pointed out in Sect. 2, all observational, model and reanalysis climate datasets are affected by various kinds of uncertainties and shortcomings. However, by comparing several state-of-the-art datasets of different origins, one can obtain a measure of the robustness of the presented results. A ubiquitous property of T_s , P , E and W spectra taken over the full globe, global-land and global-oceans for both high temporal resolution datasets (ERA-20C and 20CR) was an abrupt change in the spectral exponents, corresponding to the weather to macroweather transition previously discussed by Lovejoy (2015). The weather regime characterizes the small time-scales, where $\beta \geq 1$, and hence the amplitude of the fluctuations tends to increase or maintain with increasing time-scale. At larger time-scales, the spectra displayed significantly flatter slopes across all the considered datasets and variables. This is the macroweather regime, where the spectral slopes are $0 < \beta < 1$, and hence the fluctuations tend to decrease with increasing temporal scale (up to a few decades), thus implying a convergence towards the ‘climate normal’. Furthermore, spectral analysis showed that all the considered satellite-based products, reanalysis and climate model simulation display a generally good agreement on the representation of the macroweather regime, specifically in the spectral slopes. Notice that this agreement of the statistics over wide

range of time scales is a necessary condition for agreement between two datasets, but it is not sufficient since each dataset could represent a statistically independent realization of the same stochastic process (de Lima and Lovejoy 2015).

The weather to macroweather transition was estimated to occur at time-scales between about 10 days and 1 month for nearly all cases. The only exceptions were the spectra of T_s over the ocean (i.e. SST) and E over land, both displaying a transition at larger time-scales (around 1 year) in all the available datasets. The SST spectra is in agreement with Lovejoy (2015) theoretical prediction for the ocean weather to ocean macroweather transition scale, which should occur around 1 year due to the lower magnitude turbulent fluxes that characterize the oceans. The behavior of the land E spectra should be associated with the complex land–atmosphere interactions, including the limited moisture availability over land in contrast to the infinite oceanic source, but further work is required on this topic. At time-scales larger than a few decades, a ‘climate regime’ should emerge where the amplitude of the fluctuations increases again with time-scale (as shown for temperature by Huybers and Curry (2006) and Lovejoy (2015)). While there are some hints of this transition in the present investigation, the results should be interpreted with care given the limited record length of the considered datasets used.

All datasets also agree on the multiscale correlation structure of W against T_s , characterized by negligible correlations at time-scales below about 6 months, followed by a sharp increase to remarkably high ρ_{DCCA} values at time-scales larger than a few years, reaching values > 0.8 (often ~ 0.9) for the full globe and global ocean, and within the 0.6–0.8 range for global land. Interestingly, Lovejoy et al. (2017) found a similar behavior for the correlation between air temperature over land and over the ocean. They interpreted the high correlation multi-year time-scale range as the basic ocean/atmosphere coupling scale, itself corresponding to the transition from ocean weather to ocean macroweather. If this explanation is correct, then the transition in ρ_{DCCA} found here has important implications. At time-scales shorter than about 6 months, the ocean is not a dominant drive of atmospheric water variability, i.e. W variability is not tightly coupled to SST. This is followed by a transition zone at time-scales up to a few years, after which the atmosphere and the ocean start to act as a single coupled system. Particularly, the atmospheric water content becomes tightly coupled to the ocean surface temperature, with C–C playing the key variability mechanism.

Another robust feature across all datasets is that the C–C relationship is not the dominant variability mechanisms of P or E over land throughout the entire time-scale range considered (a few days to about a decade), as shown by negligible ρ_{DCCA} values. It is important to notice that that a weak correlation coefficient does not

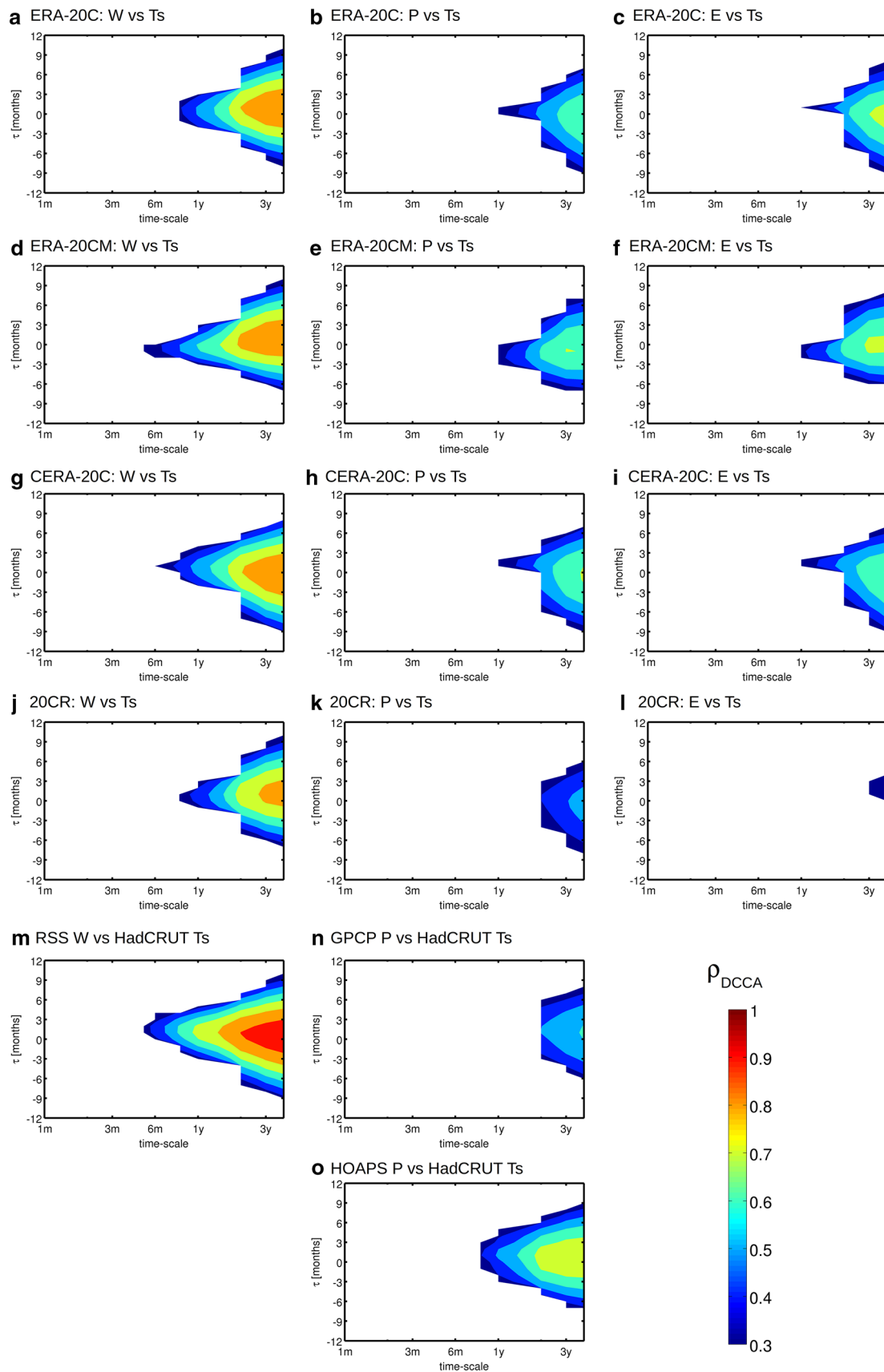


Fig. 8 Same as Fig. 7 but for time-series averaged over global ocean only

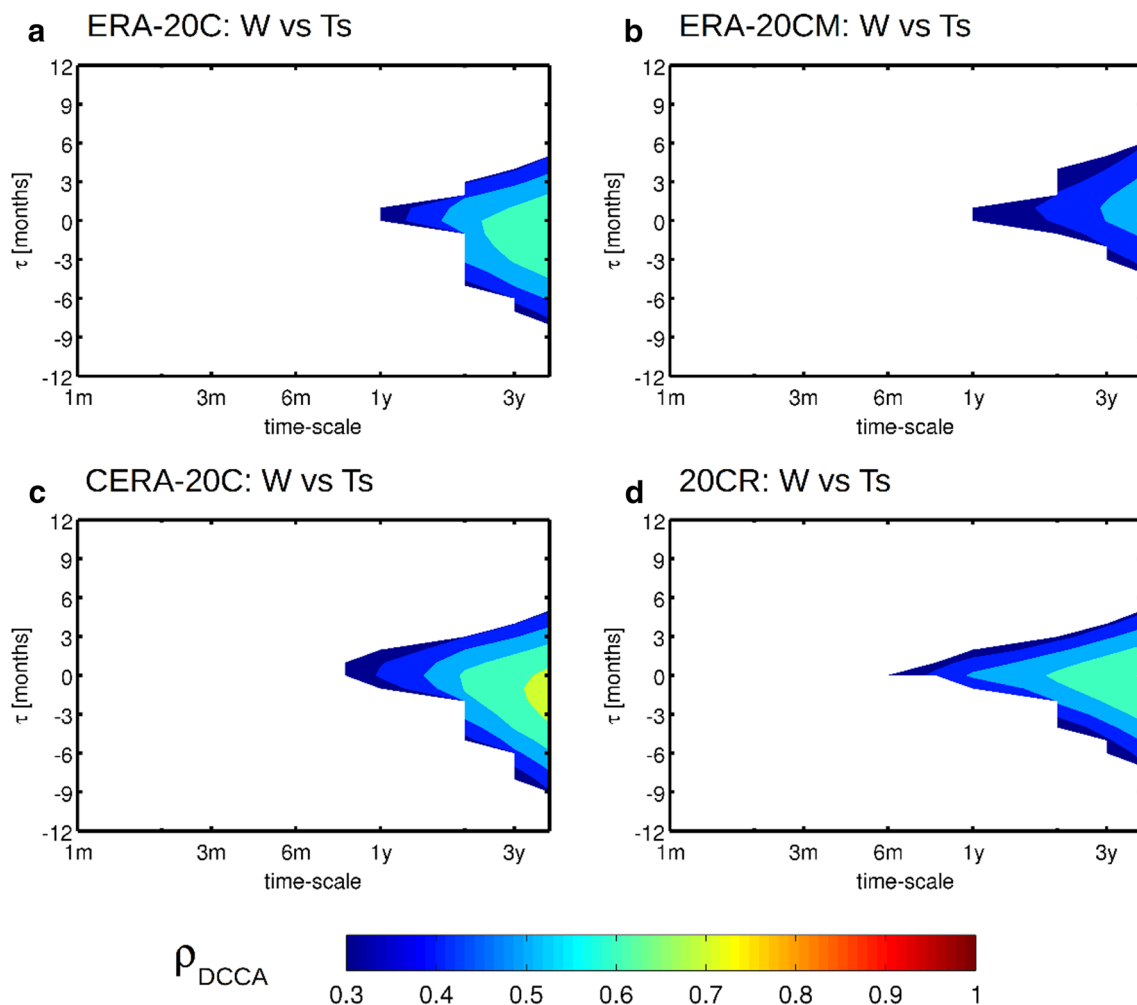


Fig. 9 Same as Fig. 7 but for time-series averaged over global land only. Notice that over land P and E do not show any significant correlations against T_s in any of the considered datasets

exclude a sensitivity of P to T_s , as pointed out by Gu and Adler (2012). Instead, it indicates the complexity of the relations between these two variables in that various forcings may work at different time-scales and the dominant mechanisms may change. For example, the generation of precipitation requires not only moisture but also instability and lifting, not all of which depends strongly on temperature. In fact, Gu and Adler (2011) and Adler et al. (2017) found different responses of precipitation to surface temperature fluctuations caused by ENSO or by large volcanic eruptions, due to differences in the respective dynamical responses, particularly in atmospheric stability. A further source of complexity comes from the non-monotonic behavior of atmospheric water content and precipitation sensitivity to temperature changes between colder and warmer climates (O’Gorman and Schneider 2008;

Schneider et al. 2010; Caballero and Hanley 2012; Levine and Boos 2016).

The multiscale structure of the correlation between P and T_s over the ocean and the full globe shows relevant differences between the different datasets considered here. On the one hand, all datasets agree that C–C is not a dominant control mechanism for the non-periodic variability of global P and E time-series at time-scales below about 6 months, displaying negligible cross-correlation coefficients between P and T_s , and E and T_s . On the other hand, the results over the global ocean and full globe show large spread amongst different datasets on the importance of C–C for P and E variability at time-scales larger than a few years, ranging from negligible correlation values (<0.3) to high correlations (between 0.6 and 0.8). This spread points to important uncertainties in the representation of the slow (macroweather) precipitation variability in the current

Table 3 Precipitable water, precipitation and evaporation sensitivity coefficients to surface temperature for global-mean, global ocean and global land averages

	α (%/K)		
	Global	Ocean	Land
Precipitable water			
ERA-20C	8	11	5
ERA-20CM	9	10	6
CERA-20C	7	9	4
20CR	10	10	7
RSS vs HadCRUT	NA	11	NA
RSS vs GISSTEMP	NA	7	NA
Precipitation			
ERA-20C	4	7	X
ERA-20CM	3	4	X
CERA-20C	3	6	X
20CR	4	6	X
GPCP vs HadCRUT	X	7	X
GPCP vs GISSTEMP	X	5	X
CMAP vs HadCRUT	X	X	X
CMAP vs GISSTEMP	X	X	X
HOAPS P vs HadCRUT	NA	7	NA
HOAPS P vs GISSTEMP	NA	11	NA
Evaporation			
ERA-20C	4	6	X
ERA-20CM	3	3	X
CERA-20C	3	5	X
20CR	X	X	X
HOAPS E vs HadCRUT	NA	X	NA
HOAPS E vs GISSTEMP	NA	X	NA

The α values are presented for all the datasets where data is available and the respective DCCA correlation coefficients are >0.4 . X means that $\rho_{DCCA} < 0.4$ and NA means that data is not available for specific variable from a dataset over that region

state-of-the-art datasets. Additionally, the results suggest that caution should be taken with the often-assumed linear sensitivity of P (or E) fluctuations to T_S (see e.g. Eq. 2) over the full globe and global-ocean averages, while this assumption is not valid for global-land. Nonetheless, the estimates of the climate sensitivity coefficients for time-scales larger than a few years, and for the cases where significant correlations exist, showed values close to the typical 7%/K derived from C–C relationship for W . For P and E the α values are slightly larger than the most often reported range of 1–3%/K. But the match improves when the worst fits associated with lower cross-correlations and/or shorter record lengths are excluded.

Finally, notice that the multi-scale correlation structure found here is not changed by considering different analysis periods (satellite period of 1900–2010); nor different climatological references periods; nor including atmospheric

liquid water content; nor using 2-m temperature, surface temperature or a combination of both (SST over the sea and T_{2m} over land); and, more importantly, it is not changed by considering the possibility of lagged-correlations, since the zero-lag value is always very close to the maximum correlation. This provides further robustness to the results presented here.

Acknowledgements This study was funded by the Portuguese Science Foundation (FCT), under Grant UID/GEO/50019/2013, as part of Research Project SOLAR (PTDC/GEOMET/7078/2014). All the datasets used in the present investigation are freely available. ERA-20C, ERA-20CM and CERA-20C products were provided by ECMWF and are available through the website <http://apps.ecmwf.int/datasets>. 20CR reanalysis, and GPCP and CMAP precipitation products were provided by the NOAA/OAR/ESRL PSD, Boulder, Colorado, USA, from their website at <http://www.esrl.noaa.gov/psd>. HOAPS precipitation and evaporation datasets were provided by EUMETSAT through the website <http://wui.cmsaf.eu>. RSS monthly mean precipitable water product was provided by Remote Sensing Systems Version-8 Microwave Radiometer Data, Santa Rosa, CA, USA, from their website <http://www.remss.com>.

References

- Adler RF et al. (2003) The version-2 global precipitation climatology project (GPCP) monthly precipitation analysis (1979–present). *J Hydrometeorol* 4(6):1147–1167. [https://doi.org/10.1175/1525-7541\(2003\)004<1147:TVGPCP>2.0.CO;2](https://doi.org/10.1175/1525-7541(2003)004<1147:TVGPCP>2.0.CO;2)
- Adler RF, Gu G, Wang J-J, Huffman GJ, Curtis S, Bolvin D (2008) Relationships between global precipitation and surface temperature on interannual and longer timescales (1979–2006). *J Geophys Res* 113:D22104. <https://doi.org/10.1029/2008JD10536>
- Adler RF, Gu G, Sapiano M et al (2017) Global precipitation: means, variations and trends during the satellite era (1979–2014). *Surv Geophys* 38:679–699. <https://doi.org/10.1007/s10712-017-9416-4>
- Allan RP, Soden BJ, John VO, Ingram W, Good P (2010) Current changes in tropical precipitation. *Environ Res Lett* 5(2):025205. <https://doi.org/10.1088/1748-9326/5/2/025205>
- Allen MR, Ingram WJ (2002) Constraints on future changes in climate and the hydrological cycle. *Nature* 419:224–232
- Andersson A et al (2010) The Hamburg ocean atmosphere parameters and fluxes from satellite data—HOAPS-3. *Earth Syst Sci Data Discuss* 3:143–194
- Barros AP, Kim G, Williams E, Nesbitt SW (2004) Probing orographic controls in the Himalayas during the monsoon using satellite imagery. *Nat Hazards Earth Syst Sci* 4(1):29–51
- Betts AK (1998) Climate-convection feedbacks: some further issues. *Clim Change* 39:35–38
- Boer GJ (1993) Climate change and the regulation of the surface moisture and energy budgets. *Clim Dyn* 8:225–239
- Bosilovich MG, Robertson FR, Takacs L, Molod A, Mocko D (2017) Atmospheric water balance and variability in the MERRA-2 reanalysis. *J Clim* 30:1177–1196. <https://doi.org/10.1175/JCLI-D-16-0338.1>
- Caballero R, Hanley J (2012) Midlatitude eddies, storm-track diffusivity, and poleward moisture transport in warm climates. *J Atmos Sci* 69:3237–3250. <https://doi.org/10.1175/JAS-D-12-035.1>
- Chenhua S (2015) Analysis of detrended time-lagged cross-correlation between two nonstationary time series. *Phys Lett A* 379:680–687. <https://doi.org/10.1016/j.physleta.2014.12.036>

- Compo GP, Whitaker JS, Sardeshmukh PD, Matsui N, Allan RJ, Yin X, Gleason BE, Vose RS, Rutledge G, Bessemoulin P, Brönnimann S, Brunet M, Crouthamel RI, Grant AN, Groisman PY, Jones PD, Kruk MC, Kruger AC, Marshall GJ, Maugeri M, Mok HY, Nordli Ø, Ross TF, Trigo RM, Wang XL, Woodruff SD, Worley SJ (2011) The twentieth century reanalysis project. *Q J R Meteorol Soc* 137:1–28. <https://doi.org/10.1002/qj.776>
- de Lima MIP, Lovejoy S (2015) Macroweather precipitation variability up to global and centennial scales. *Water Resour Res* 51:9490–9513. <https://doi.org/10.1002/2015WR017455>
- Fraedrich K, Blender R (2003) Scaling of atmosphere and ocean temperature correlations in observations and climate models. *Phys Rev Lett* 90:108510. <https://doi.org/10.1103/PhysRevLett.90.108510>
- Fredriksen H, Rypdal K (2016) Spectral characteristics of instrumental and climate model surface temperatures. *J Clim* 29:1253–1268. <https://doi.org/10.1175/JCLI-D-15-0457.1>
- Gehne M, Hamill TM, Kiladis GN, Trenberth KE (2016) Comparison of global precipitation estimates across a range of temporal and spatial scales. *J Clim* 29:7773–7795. <https://doi.org/10.1175/JCLI-D-15-0618.1>
- Gu G, Adler RF (2011a) Precipitation and temperature variations on the interannual time scale: assessing the impact of ENSO and volcanic eruptions. *J Clim* 24:2258–2270
- Gu G, Adler RF (2012) Large-scale, inter-annual relations among surface temperature, water vapour and precipitation with and without ENSO and volcano forcings. *Int J Climatol* 32:1782–1791. <https://doi.org/10.1002/joc.2393>
- Gu G, Adler RF (2013) Interdecadal variability/long-term changes in global precipitation patterns during the past three decades: global warming and/or Pacific decadal variability? *Clim Dyn* 40:3009–3022. <https://doi.org/10.1007/s00382-012-1443-8>
- Gu G, Adler RF, Huffman GJ, Curtis S (2007) Tropical rainfall variability on interannual-to-interdecadal and longer time scales derived from the GPCP monthly product. *J Clim* 20:4033–4046. <https://doi.org/10.1175/JCLI4227.1>
- Gutowski WJ, Decker SG, Donavon RA, Pan Z, Arritt RW, Takle ES (2003) Temporal-spatial scales of observed and simulated precipitation in central US climate. *J Clim* 16:3841–3847. [https://doi.org/10.1175/1520-0442\(2003\)0163841:T00AS2.0.CO;2](https://doi.org/10.1175/1520-0442(2003)0163841:T00AS2.0.CO;2)
- Hansen J, Ruedy R, Sato M, Lo K (2010) Global surface temperature change. *Rev Geophys* 48:RG4004. <https://doi.org/10.1029/2010RG000345>
- Held IM, Soden BJ (2006) Robust responses of the hydrological cycle to global warming. *J Clim* 19:5686–5699
- Henriksson SV et al (2015) Improved power-law estimates from multiple samples provided by millennium climate simulations. *Theor Appl Climatol* 119:667–677. <https://doi.org/10.1007/s00704-014-1132-0>
- Hersbach H, Peubey C, Simmons A, Berrisford P, Poli P, Dee DP (2015) ERA-20CM: a twentieth century atmospheric model ensemble. *Q J R Meteorol Soc* 141:2350–2375. <https://doi.org/10.1002/qj.2528>
- Horvatic D, Stanley HE, Podobnik B (2011) Detrended cross-correlation analysis for non-stationary time-series with periodic trends. *Europhys Lett* 94:18007
- Huybers P, Curry W (2006) Links between annual, Milankovitch and continuum temperature variability. *Nature* 441:329–332
- Kantelhardt JW, Zschiegner SA, Koscielny-Bunde E, Havlin S, Bunde A, Stanley HE (2002) Multifractal detrended fluctuation analysis of nonstationary time-series. *Phys A* 316:87–114
- Kidd C, Bauer P, Turk J, Huffman GJ, Joyce R, Hsu KL, Braithwaite D (2012) Inter-comparison of high-resolution precipitation products over northwest Europe. *J Hydrometeorol* 13(1):67–83. <https://doi.org/10.1175/JHM-D-11-042.1>
- Laloyaux P, Balmaseda M, Dee D, Mogensen K, Janssen P (2016) A coupled data assimilation system for climate reanalysis. *QJR Meteorol Soc* 142:65–78. <https://doi.org/10.1002/qj.2629>
- Levine XJ, Boos WR (2016) A mechanism for the response of the zonally asymmetric subtropical hydrologic cycle to global warming. *J Clim* 29:7851–7867. <https://doi.org/10.1175/JCLI-D-15-0826.1>
- Liu C, Allan RP (2012) Multisatellite observed responses of precipitation and its extremes to interannual climate variability. *J Geophys Res* 117:D03101. <https://doi.org/10.1029/2011JD016568>
- Lorenz C, Kunstmann H (2012) The hydrological cycle in three-state-of-the-art reanalyses: intercomparison and performance analysis. *J Hydrometeorol* 13:1397–1420. <https://doi.org/10.1175/JHM-D-11-088.1>
- Lovejoy S (2015) A voyage through scales, a missing quadrillion and why the climate is not what you expect. *Clim Dyn* 44:3187–3210
- Lovejoy S, Schertzer D (2013) *The weather and climate: emergent laws and multifractal cascades*. Cambridge University Press, Cambridge
- Lovejoy S, Del Rio Amador L, Hébert R (2017) Harnessing butterflies: theory and practice of the stochastic seasonal to interannual prediction system (StocSIPS). In: Tsonis A (ed) *Advances in nonlinear geosciences*. Springer, Cham
- Morice CP, Kennedy JJ, Rayner NA, Jones PD (2012) Quantifying uncertainties in global and regional temperature change using an ensemble of observational estimates: the HadCRUT4 dataset. *J Geophys Res* 117:D08101. <https://doi.org/10.1029/2011JD017187>
- Nogueira M (2017a) Exploring the link between multiscale entropy and fractal scaling behavior in near-surface wind. *PLoS One* 12(3):e0173994. <https://doi.org/10.1371/journal.pone.0173994>
- Nogueira M (2017b) Exploring the links in monthly to decadal variability of the atmospheric water balance over the wettest regions in ERA-20C. *J Geophys Res Atmos*. <https://doi.org/10.1002/2017JD027012>
- Nogueira M, Barros AP (2015) Transient stochastic downscaling of quantitative precipitation estimates for hydrological applications. *J Hydrol* 529(3):1407–1421
- O’Gorman PA, Muller CG (2010) How closely do changes in surface and column water vapour follow Clausius–Clapeyron scaling in climate change simulations? *Environ Res Lett* 5:025207
- O’Gorman PA, Schneider T (2008) The hydrological cycle over a wide range of climates simulated with an idealized GCM. *J Clim* 21:3815–3832. <https://doi.org/10.1175/2007JCLI2065.1>
- Pelletier J (2002) Natural variability of atmospheric temperatures and geomagnetic intensity over a wide range of time scales. *PNAS* 99:2546–2553
- Piao L, Fu Z (2016) Quantifying distinct associations on different temporal scales: comparison of DCCA and Pearson methods. *Sci Rep* 6:36759. <https://doi.org/10.1038/srep36759>
- Podobnik B, Stanley HE (2008) Detrended cross-correlation analysis: a new method for analyzing nonstationary time-series. *Phys Rev Lett* 100:084102
- Podobnik B, Jiang Z, Zhou W, Stanley HE (2011) Statistical tests for power-law cross-correlated processes. *Phys Rev E* 84:066118
- Poli P et al (2016) ERA-20C: an atmospheric reanalysis of the twentieth century. *J Clim* 29:4083–4097. <https://doi.org/10.1175/JCLI-D-15-0556.1>
- Rybski D, Bunde A, von Storch H (2008) Long-term memory in 1000-year simulated temperature records. *J Geophys Res* 113:D02106. <https://doi.org/10.1029/2007JD008568>
- Schneider T, O’Gorman PA, Levine XJ (2010) Water vapor and the dynamics of climate changes. *Rev Geophys* 48:RG3001. <https://doi.org/10.1029/2009RG000302>
- Singleton A, Toumi R (2013) Super-Clausius–Clapeyron scaling of rainfall in a model squall line. *Q J R Meteorol Soc* 139:334–339

- Sohn BJ, Han H-J, Seo E-K (2010) Validation of satellite-based high-resolution rainfall products over the Korean peninsula using data from a dense rain gauge network. *J Appl Meteor Climatol* 49(4):701–714. <https://doi.org/10.1175/2009JAMC2266.1>
- Stephens GL, Ellis TD (2008) Controls of global-mean precipitation increases in global warming GCM experiments. *J Clim* 21:6141–6155. <https://doi.org/10.1175/2008JCLI2144.1>
- Trenberth KE (1998) Atmospheric moisture residence times and cycling: implications for rainfall rates with climate change. *Clim Change* 39:667–694
- Trenberth KE (2011) Changes in precipitation with climate change. *Clim Res* 47:123–138
- Trenberth KE, Fasullo J, Smith L (2005) Trends and variability in column-integrated atmospheric water vapor. *Clim Dyn* 24:741–758
- Trenberth KE, Fasullo JT, Mackaro J (2011) Atmospheric moisture transports from ocean to land and global energy flows in reanalyses. *J Clim* 24:4907–4924. <https://doi.org/10.1175/2011JCLI4171.1>
- Vyushin DI, Kushner PJ (2009) Power-law and long-memory characteristics of the atmospheric general circulation. *J Clim* 22:2890–2904
- Vyushin DI, Kushner PJ, Mayer J (2009) On the origins of temporal power-law behavior in the global atmospheric circulation. *Geophys Res Lett* 36:L14706. <https://doi.org/10.1029/2009GL038771>
- Wentz FJ (1997) A well-calibrated ocean algorithm for SSM/I. *J Geophys Res* 102(C4):8703–8718
- Wentz FJ, Schabel M (2000) Precise climate monitoring using complementary satellite data sets. *Nature* 403:414–416
- Wentz F, Ricciardulli L, Mears C (2007) How much more rain will global warming bring? *Science* 317:233–235
- Whitaker JS, Hamill TM (2002) Ensemble data assimilation without perturbed observations. *Mon Weather Rev* 130:1913–1924. [https://doi.org/10.1175/1520-0493\(2002\)130<1913:EDAWPO>2.0.CO;2](https://doi.org/10.1175/1520-0493(2002)130<1913:EDAWPO>2.0.CO;2)
- Xie P, Arkin PA (1997) Global precipitation: a 17-year monthly analysis based on gauge observations, satellite estimates, and numerical model outputs. *Bull Am Meteorol Soc* 78:2539–2558